



ELSEVIER

Physica A 273 (1999) 452–475

**PHYSICA** A

www.elsevier.com/locate/physa

# Quantitative analysis of experimental and synthetic microstructures for sedimentary rock

B. Biswal<sup>a,b</sup>, C. Manwart<sup>a</sup>, R. Hilfer<sup>a,c,\*</sup>, S. Bakke<sup>d</sup>, P.E. Øren<sup>d</sup>

<sup>a</sup>*ICA-1, Universität Stuttgart, Pfaffenwaldring 27, 70569 Stuttgart, Germany*

<sup>b</sup>*Department of Physics & Electronics, Sri Venkateswara College, University of Delhi, New Delhi 110 021, India*

<sup>c</sup>*Institut für Physik, Universität Mainz, 55099 Mainz, Germany*

<sup>d</sup>*Statoil Research Center, 7004 Trondheim, Norway*

Received 17 May 1999

---

## Abstract

A quantitative comparison between the experimental microstructure of a sedimentary rock and three theoretical models for the same rock is presented. The microstructure of the rock sample (Fontainebleau sandstone) was obtained by microtomography. Two of the models are stochastic models based on correlation function reconstruction, and one model is based on sedimentation, compaction and diagenesis combined with input from petrographic analysis. The porosity of all models closely match that of the experimental sample and two models have also the same two point correlation function as the experimental sample. We compute quantitative differences and similarities between the various microstructures by a method based on local porosity theory. Differences are found in the degree of anisotropy, and in fluctuations of porosity and connectivity. The stochastic models differ strongly from the real sandstone in their connectivity properties, and hence need further refinement when used to model transport. © 1999 Elsevier Science B.V. All rights reserved.

*PACS:* 61.43.G; 81.05.Rm; 47.55.Mh

---

## 1. Introduction

A quantitative prediction of fluid flow, sound propagation, or chemical transport in strongly correlated disordered media, such as sedimentary rock, frequently employs representative microscopic models of the microstructure as input. A large number of microscopic models have been proposed over the years to represent the microstructure of porous media [1–15].

---

\* Corresponding author. Inst. für Computeranwendungen 1, Pfaffenwaldring 27, 70569 Stuttgart, Germany.

Microscopic models do not reproduce the exact microstructure of the medium at hand, but are based on the idea that the experimental sample is a representative realization drawn from a statistical ensemble of similar microstructures. Hence it is necessary to have methods for distinguishing microstructures quantitatively [16–19]. This is particularly important for attempts to generate porous microstructures in an automatic computerized process [9,20–22,10].

Despite the generality of the problem sketched above our discussion will be focussed on fluid flow through sedimentary rocks. In particular we will discuss Fontainebleau sandstone. This model system has (together with Berea sandstone) acquired the status of a reference standard for modeling and analysing sedimentary rocks [9–23,25,21].

General geometric characterization methods traditionally include porosities, specific surface areas, and sometimes correlation functions [2,9,26–28]. Recently a more refined, quantitative characterization for general stochastic microstructures was based on local porosity theory (LPT) [16,18,29,30–35]. LPT is currently the most general geometric characterization method because it contains as a special case also the characterization through correlation functions (see [16] for details).

Local porosity theory is used in this paper to distinguish quantitatively various models for Fontainebleau sandstone. More precisely, the objective of this work is to give a quantitative comparison of four microstructures. One of them is an experimental sample of Fontainebleau sandstone, while three of the microstructures are synthetic samples from computer simulation models for Fontainebleau sandstone. One of the models is a sedimentation and diagenesis model that tries to mimick the formation of sandstone through deposition and cementation of spherical grains. Two purely stochastic models generate random realizations of microstructures with prescribed porosity and correlation function. The first of these is based on Fourier space filtering of Gaussian random fields, and the second is based on a simulated annealing algorithm.

In Section 2 we introduce and define the geometrical quantities that will be used to distinguish the microstructures. In Section 3 we present the four microstructures, their generation and characterization in terms of the generation procedure. In Section 4 we present the results and discuss the differences between the four microstructures.

## 2. Measured quantities

### 2.1. Porosity and correlation functions

Consider a rock sample occupying a subset  $\mathbb{S} \subset \mathbb{R}^d$  of the physical space ( $d = 3$  in the following). The sample  $\mathbb{S}$  contains two disjoint subsets  $\mathbb{S} = \mathbb{P} \cup \mathbb{M}$  with  $\mathbb{P} \cap \mathbb{M} = \emptyset$  where  $\mathbb{P}$  is the pore space and  $\mathbb{M}$  is the rock or mineral matrix and  $\emptyset$  is the empty set. The porosity  $\phi(\mathbb{S})$  of such a two component porous medium is defined as the ratio  $\phi(\mathbb{S}) = V(\mathbb{P})/V(\mathbb{S})$  which gives the volume fraction of pore space. Here  $V(\mathbb{P})$  denotes the volume of the pore space, and  $V(\mathbb{S})$  is the total sample volume.

For the sample data analysed here the set  $\mathbb{S}$  is a rectangular parallelepiped whose sidelengths are  $M_1, M_2$  and  $M_3$  in units of the lattice constant  $a$  (resolution) of a simple cubic lattice. Thus the sample is represented in practice as the subset  $\mathbb{S} = [0, M_1 - 1] \times [0, M_2 - 1] \times [0, M_3 - 1] \subset \mathbb{Z}^3$  of an infinite cubic lattice.  $\mathbb{Z}$  denotes the set of integers, and  $[0, M_i - 1] \subset \mathbb{Z}$  are intervals. The position vectors  $\mathbf{r}_i = \mathbf{r}_{i_1, \dots, i_d} = (ai_1, \dots, ai_d)$  with integers  $0 \leq i_j < M_j$  are used to label the voxels, and  $\mathbf{r}_i$  is a shorthand notation for  $\mathbf{r}_{i_1, \dots, i_d}$ . A configuration (or microstructure)  $\mathcal{Z}$  of a 2-component medium is then given as

$$\mathcal{Z} = (Z_1, \dots, Z_N) = (\chi_{\mathbb{P}}(\mathbf{r}_1), \dots, \chi_{\mathbb{P}}(\mathbf{r}_N)), \tag{2.1}$$

where  $N = M_1 M_2 M_3$ , and

$$\chi_{\mathbb{G}}(\mathbf{r}) = \begin{cases} 1 & \text{for } \mathbf{r} \in \mathbb{G}, \\ 0 & \text{for } \mathbf{r} \notin \mathbb{G} \end{cases} \tag{2.2}$$

is the characteristic (or indicator) function of a set  $\mathbb{G}$  that indicates when a point is inside or outside of  $\mathbb{G}$ . A stochastic medium is defined through the discrete probability density

$$p(z_1, \dots, z_N) = \text{Prob}\{(Z_1 = z_1) \wedge \dots \wedge (Z_N = z_N)\} \tag{2.3}$$

where  $z_i \in \{0, 1\}$ . Expectation values of functions  $f(\mathcal{Z}) = f(z_1, \dots, z_N)$  are defined as

$$\langle f(z_1, \dots, z_N) \rangle = \sum_{z_1=0}^1 \dots \sum_{z_N=0}^1 f(z_1, \dots, z_N) p(z_1, \dots, z_N), \tag{2.4}$$

where the summations run over all configurations. If the medium is statistically homogeneous (stationary) then the average porosity is given as

$$\langle \phi \rangle = \text{Prob}\{\mathbf{r}_0 \in \mathbb{P}\} = \langle \chi_{\mathbb{P}}(\mathbf{r}_0) \rangle, \tag{2.5}$$

where  $\mathbf{r}_0$  is an arbitrary lattice site. If the medium is also ergodic then the limit

$$\lim_{N \rightarrow \infty} \phi(\mathbb{S}) = \langle \phi \rangle \tag{2.6}$$

exists. There are, however, many subtleties associated with this limit (see [16] for details). Finally, we now define the correlation function for a homogeneous medium as the expectation

$$G(\mathbf{r}_0, \mathbf{r}) = G(\mathbf{r} - \mathbf{r}_0) = \frac{\langle \chi_{\mathbb{P}}(\mathbf{r}_0) \chi_{\mathbb{P}}(\mathbf{r}) \rangle - \langle \phi \rangle^2}{\langle \phi \rangle (1 - \langle \phi \rangle)}. \tag{2.7}$$

If the medium is also isotropic  $G(\mathbf{r}) = G(|\mathbf{r}|) = G(r)$ . Obviously,  $G(0) = 1$  and  $G(\infty) = 0$ .

### 2.2. Local porosity distributions

The basic idea of local porosity theory is to measure geometric observables within a bounded (compact) subset of the porous medium and to collect these measurements into various histograms. Let  $\mathbb{K}(\mathbf{r}, L)$  denote a cube of sidelength  $L$  centered at the lattice vector  $\mathbf{r}$ . The set  $\mathbb{K}(\mathbf{r}, L)$  defines a measurement cell inside of which local geometric properties such as porosity or specific internal surface are measured [30]. The local porosity in this measurement cell  $\mathbb{K}(\mathbf{r}, L)$  is defined as

$$\phi(\mathbf{r}, L) = \frac{V(\mathbb{P} \cap \mathbb{K}(\mathbf{r}, L))}{V(\mathbb{K}(\mathbf{r}, L))}, \tag{2.8}$$

where  $V(\mathbb{G})$  is the volume of the set  $\mathbb{G} \subset \mathbb{R}^d$ . The local porosity distribution  $\mu(\phi, L)$  is defined as

$$\mu(\phi, L) = \frac{1}{m} \sum_{\mathbf{r}} \delta(\phi - \phi(\mathbf{r}, L)), \tag{2.9}$$

where  $m$  is the number of placements of the measurement cell  $\mathbb{K}(\mathbf{r}, L)$  and  $\delta(x)$  is Dirac’s  $\delta$ -distribution. Ideally all measurement cells should be disjoint [30], but in practice this cannot be achieved because of poor statistics. The results presented below are obtained by placing  $\mathbb{K}(\mathbf{r}, L)$  on all lattice sites  $\mathbf{r}$  which are at least a distance  $L/2$  from the boundary of  $\mathbb{S}$ , and hence the following equation

$$m = \prod_{i=1}^3 (M_i - L + 1) \tag{2.10}$$

will be used.  $\mu(\phi, L)$  is the empirical probability density function (histogram) of local porosities. Its support is the unit interval. In the following we denote averages with respect to  $\mu(\phi, L)$  by an overline. Thus for a homogeneous and ergodic medium

$$\bar{\phi}(L) = \int_0^1 \phi \mu(\phi, L) d\phi = \langle \phi \rangle \tag{2.11}$$

is the expected local porosity. In practice deviations from the last equality may occur if the measurement cells are overlapping. Fig. 10 shows the average local porosity as function of  $L$  for all four samples analyzed in this paper showing that deviations can be as large as 0.5%. The deviations may be partly intrinsic and partly due to oversampling the central regions because the measurement cells are overlapping. Similarly the variance of local porosities is found as [16]

$$\begin{aligned} \sigma^2(L) &= \overline{(\phi(L) - \bar{\phi}(L))^2} = \int_0^1 [\phi - \bar{\phi}(L)]^2 \mu(\phi, L) d\phi \\ &= \frac{1}{L^3} \langle \phi \rangle (1 - \langle \phi \rangle) \left( 1 + \frac{2}{L^3} \sum_{\substack{\mathbf{r}_i, \mathbf{r}_j \in \mathbb{K}(\mathbf{r}_0, L) \\ i \neq j}} G(\mathbf{r}_i - \mathbf{r}_j) \right), \end{aligned} \tag{2.12}$$

where  $\mathbb{K}(\mathbf{r}_0, L)$  is any cubic measurement cell.

Table 1  
Legend for index  $\alpha$  of local percolation probabilities  $\lambda_\alpha(\phi, L)$

Index $\alpha$	Meaning
$x$	$x$ -direction
$y$	$y$ -direction
$z$	$z$ -direction
$3$	$(x \wedge y \wedge z)$ -direction
$c$	$(x \vee y \vee z)$ -direction

It is simple to determine  $\mu(\phi, L)$  in the limits  $L \rightarrow 0$  and  $L \rightarrow \infty$  of small and large measurement cells. For small cells one finds generally [30,16]

$$\mu(\phi, L = 0) = \phi(\mathbb{S})\delta(\phi - 1) + (1 - \phi(\mathbb{S}))\delta(\phi), \tag{2.13}$$

where  $\phi(\mathbb{S})$  is the sample porosity. If the sample is macroscopically homogeneous and ergodic then one expects

$$\mu(\phi, L \rightarrow \infty) = \delta(\phi - \phi(\mathbb{S})), \tag{2.14}$$

indicating that in both limits the geometrical information contained in  $\mu(\phi, L)$  consists of the single number  $\phi(\mathbb{S})$ . The macroscopic limit, however, involves the question of macroscopic heterogeneity versus macroscopic homogeneity (for more information see [16]). In any case, if Eqs. (2.13) and (2.14) hold it follows that there exists a special length scale  $L^*$  defined as

$$L^* = \min\{L: \mu(0, L) = \mu(1, L) = 0\} \tag{2.15}$$

at which the  $\delta$ -distributions at  $\phi = 0$  and  $1$  both vanish simultaneously for the first time.

### 2.3. Local percolation probabilities

The local percolation probabilities characterize the connectivity of measurement cells of a given local porosity. Let

$$A_\alpha(\mathbf{r}, L) = \begin{cases} 1 & \text{if } \mathbb{K}(\mathbf{r}, L) \text{ percolates in “}\alpha\text{”-direction} \\ 0 & \text{otherwise} \end{cases} \tag{2.16}$$

be an indicator for percolation. What is meant by “ $\alpha$ ”-direction is summarized in Table 1. A cell  $\mathbb{K}(\mathbf{r}, L)$  is called “percolating in the  $x$ -direction” if there exists a path inside the set  $\mathbb{P} \cap \mathbb{K}(\mathbf{r}, L)$  connecting those two faces of  $\mathbb{S}$  that are vertical to the  $x$ -axis. Similarly for the other directions. Thus,  $A_3 = 1$  indicates that the cell can be traversed along all 3 directions, while  $A_c = 1$  indicates that there exists at least one direction along which the block is percolating.

The local percolation probability in the “ $\alpha$ ”-direction is now defined through

$$\lambda_\alpha(\phi, L) = \frac{\sum_{\mathbf{r}} A_\alpha(\mathbf{r}, L) \delta_{\phi\phi(\mathbf{r}, L)}}{\sum_{\mathbf{r}} \delta_{\phi\phi(\mathbf{r}, L)}}, \tag{2.17}$$

where  $\delta_{\phi\phi(\mathbf{r},L)} = 1$  if  $\phi = \phi(\mathbf{r},L)$  and 0 otherwise. The local percolation probability  $\lambda_{\alpha}(\phi,L)$  gives the fraction of measurement cells of sidelength  $L$  with local porosity  $\phi$  that are percolating in the “ $\alpha$ ”-direction.

#### 2.4. Total fraction of percolating cells

The total fraction of all cells of size percolating along the “ $\alpha$ ”-direction is given by integration over all local porosities as

$$p_{\alpha}(L) = \int_0^1 \mu(\phi,L)\lambda_{\alpha}(\phi,L) d\phi. \quad (2.18)$$

This quantity provides an important characteristic for constructing equivalent network models. It gives the fraction of network elements (bond, sites etc.) which have to be permeable in an equivalent network.

### 3. Description of microstructures

#### 3.1. Experimental sample of Fontainebleau sandstone

The experimental sample is a three-dimensional microtomographic image of Fontainebleau sandstone. This sandstone is a popular reference standard because of its exceptional chemical, crystallographic and microstructural simplicity [23,24]. Fontainebleau sandstone consists of monocrystalline quartz grains that have been eroded for long periods before being deposited in dunes along the shore during the Oligocene, i.e. roughly 30 million years ago. It is well sorted containing grains of around 200  $\mu\text{m}$  in diameter. During its geological evolution, that is still not fully understood, the sand was cemented by silica crystallizing around the grains. Fontainebleau sandstone exhibits intergranular porosity ranging from 0.03 to roughly 0.3 [24].

The computer-assisted microtomography was carried out on a micro-plug drilled from a larger original core. The original core from which the micro-plug was taken had a porosity of 0.1484, a permeability of 1.3D and a formation factor of 22.1. The porosity  $\phi(\mathbb{S}_{\text{EX}})$  of our microtomographic data set is only 0.1355 (see Table 2). The difference between the porosity of the original core and that of the final data set is due to the heterogeneity of the sandstone and to the difference in sample size. The experimental sample is referred to as EX in the following. The pore space of the experimental sample is visualized in Fig. 1.

#### 3.2. Sedimentation, compaction and diagenesis model

The sedimentation, compaction and diagenesis model, abbreviated as DM in the following, is obtained by numerically modelling the main geological sandstone-forming processes [15,28]. Image analysis of backscattered electron/cathodo-luminescence images of thin sections provides input data such as porosity, grain size distribution, a

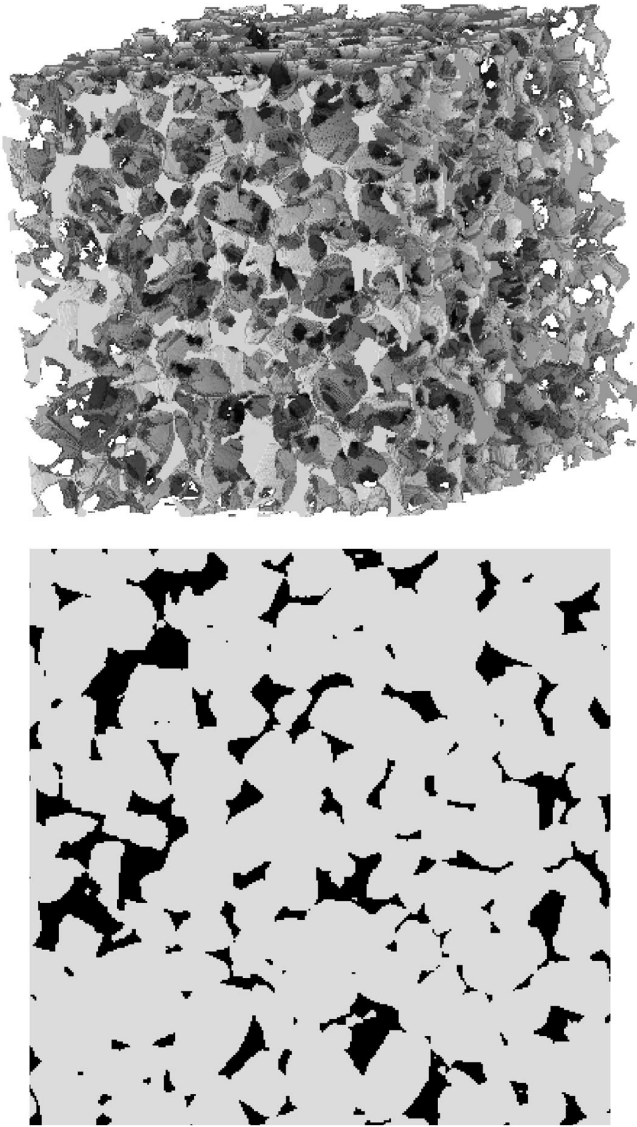


Fig. 1. Three-dimensional pore space of Fontainebleau sandstone (sample EX). The resolution of the image is  $a = 7.5 \mu\text{m}$ , the sample dimensions are  $M_1 = 300$ ,  $M_2 = 300$ ,  $M_3 = 299$ . The porosity is  $\phi(\mathbb{S}_{\text{EX}}) = 0.1355$ . The pore space is indicated opaque, the matrix space is transparent. The lower image shows the front plane of the sample as a two-dimensional thin section (pore space black, matrix grey).

visual estimate of the degree of compaction, the amount of quartz cement and clay contents and texture. The sandstone modelling is carried out in three main steps: grain sedimentation, compaction and diagenesis. Here we give only a rough sketch of the algorithms and refer the reader to [15,28] for a detailed description.

Grain sedimentation commences with image analysis of thin sections. The grain size distribution is measured using an erosion-dilation algorithm. Spherical grains with random diameters chosen from the grain size distribution are dropped onto the grain bed and relaxed into a potential energy minimum. The sedimentation environment may be low-energy (local minimum) or high-energy (global minimum).

Compaction reduces the bulk volume (and porosity) in response to vertical stress from the overburden. It is modelled here as a linear process in which the vertical coordinate of every sandgrain is shifted vertically downwards by an amount proportional to the original vertical position. The proportionality constant is called the compaction factor. Its value for our Fontainebleau sandstone is estimated to be 0.1 from thin section analysis.

In the diagenesis part only a subset of known diagenetical processes are simulated, namely quartz cement overgrowth and precipitation of authigenic clay on the free surface. Quartz cement overgrowth is modelled by radially enlarging each grain. If  $R_0$  denotes the radius of the originally deposited spherical grain, its new radius along the direction  $\mathbf{r}$  from grain centre is taken to be [7,15]

$$R(\mathbf{r}) = R_0 + \min(a\ell(\mathbf{r})^\gamma, \ell(\mathbf{r})), \quad (3.1)$$

where  $\ell(\mathbf{r})$  is the distance between the surface of the original spherical grain and the surface of its Voronoi polyhedron along the direction  $\mathbf{r}$ . The constant  $a$  controls the amount of cement, and the growth exponent  $\gamma$  controls the type of cement overgrowth. For  $\gamma > 0$  the cement grows preferentially into the pore bodies, for  $\gamma = 0$  it grows concentrically, and for  $\gamma < 0$  quartz cement grows towards the pore throats [15]. Authigenic clay growth is simulated by precipitating clay voxels on the free mineral surface. The clay texture may be pore-lining or pore-filling or a combination of the two.

For modelling the Fontainebleau sandstone we used a compaction factor of 0.1, and the cementation parameters  $\gamma = -0.6$  and  $a = 2.9157$ . The resulting configuration of our sample **DM** is displayed in Fig. 2.

### 3.3. Gaussian field reconstruction model

The Gaussian field (GF) reconstruction model provides a random pore space configuration in such a way that its correlation function  $G_{GF}(\mathbf{r})$  equals a prescribed reference correlation function  $G_0(\mathbf{r})$ . In our case  $G_0(\mathbf{r}) = G_{EX}(\mathbf{r})$  the reference is the correlation function of the experimental sample described above. The method of Gaussian field reconstruction is well documented in the literature [20,36,9,37], and we shall only make a few remarks that the reader may find of interest when implementing the method.

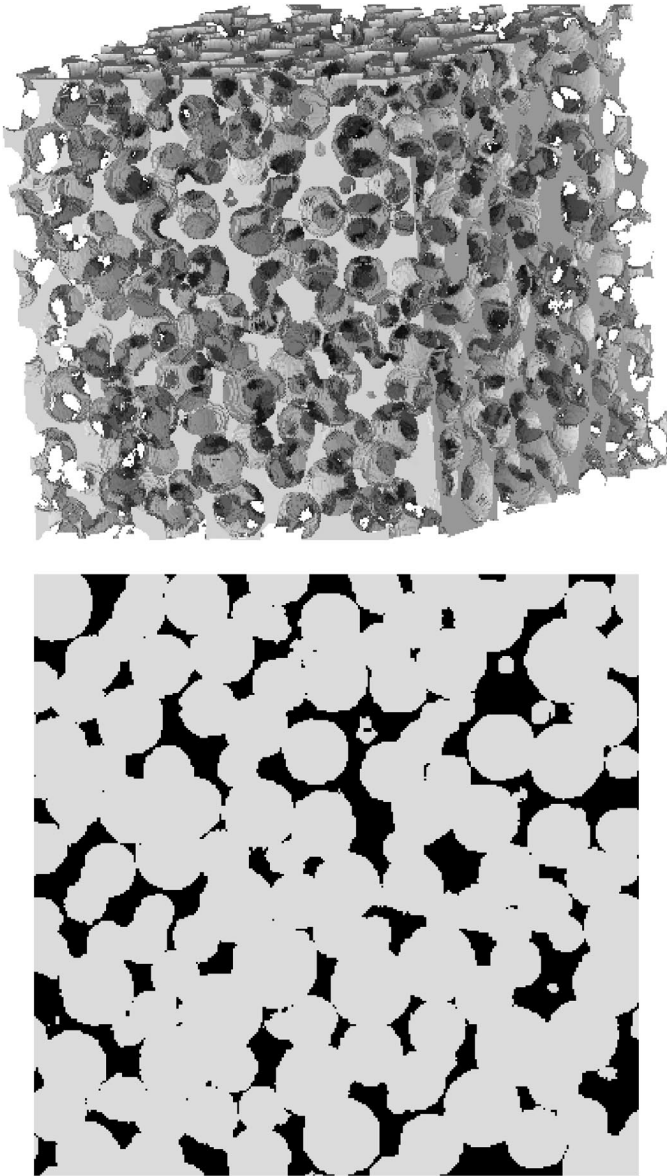


Fig. 2. Three-dimensional pore space of the sedimentation and diagenesis model (sample DM). The resolution is  $a = 7.5 \mu\text{m}$ , the sample dimensions are  $M_1 = 255$ ,  $M_2 = 255$ ,  $M_3 = 255$ . The porosity is  $\phi(\mathbb{S}_{\text{DM}}) = 0.1356$ . The pore space is indicated opaque, the matrix space is transparent. The lower image shows the front plane of the sample as a two-dimensional thin section (pore space black, matrix grey).

Given the reference correlation function  $G_{EX}(\mathbf{r})$  and porosity  $\phi(\mathbb{S}_{EX})$  of the experimental sample the three main steps of constructing the sample  $\mathbb{S}_{GF}$  with correlation function  $G_{GF}(\mathbf{r}) = G_{EX}(\mathbf{r})$  are as follows:

(1) A standard Gaussian field  $X(\mathbf{r})$  is generated which consists of statistically independent Gaussian random variables  $X \in \mathbb{R}$  at each lattice point  $\mathbf{r}$ .

(2) The field  $X(\mathbf{r})$  is first passed through a linear filter which produces a correlated Gaussian field  $Y(\mathbf{r})$  with zero mean and unit variance. The reference correlation function  $G_{EX}(\mathbf{r})$  and porosity  $\phi(\mathbb{S}_{EX})$  enter into the mathematical construction of this linear filter.

(3) The correlated field  $Y(\mathbf{r})$  is then passed through a nonlinear discretization filter which produces the reconstructed sample  $\mathbb{S}_{GF}$ .

Details of these three main steps are documented in Refs. [20,36]. However, in these traditional methods the process described in step 2 is computationally difficult because it requires the solution of a very large set of non-linear equations. We have followed an alternate and computationally more efficient method proposed in Ref. [9] which uses Fourier Transforms. For the sake of completeness we briefly describe this. Later we shall discuss some of the difficulties experienced while implementing this.

In the Fourier transform method the linear filter in step 2 is defined in Fourier space through

$$Y(\mathbf{k}) = \alpha(G_Y(\mathbf{k}))^{1/2}X(\mathbf{k}), \tag{3.2}$$

where  $M = M_1 = M_2 = M_3$  is the sidelength of a cubic sample,  $\alpha = M^{d/2}$  is the normalisation factor, and

$$X(\mathbf{k}) = \frac{1}{M^d} \sum_{\mathbf{r}} X(\mathbf{r})e^{2\pi i \mathbf{k} \cdot \mathbf{r}}, \tag{3.3}$$

denotes the Fourier transform of  $X(\mathbf{r})$ . Similarly,  $Y(\mathbf{k})$  is the Fourier transform of  $Y(\mathbf{r})$ , and  $G_Y(\mathbf{k})$  is the Fourier transform of the correlation function  $G_Y(\mathbf{r})$ .  $G_Y(\mathbf{r})$  has to be computed by an inverse process from the correlation function  $G_{EX}(\mathbf{r})$  and porosity of the experimental reference (details in [9]).

It is important to note that the Gaussian field reconstruction requires a large separation  $\zeta_{EX} \ll N^{1/d}$  where  $\zeta_{EX}$  is the correlation length of the experimental reference, and  $N = M_1 M_2 M_3$  is the number of sites.  $\zeta_{EX}$  is defined as the length such that  $G_{EX}(r) \approx 0$  for  $r > \zeta_{EX}$ . If the condition  $\zeta_{EX} \ll N^{1/d}$  is violated then step 2 of the reconstruction fails in the sense that the correlated Gaussian field  $Y(\mathbf{r})$  does not have zero mean and unit variance. In such a situation the filter  $G_Y(\mathbf{k})$  will differ from the Fourier transform of the correlation function of the  $Y(\mathbf{r})$ . It is also difficult to calculate  $G_Y(r)$  accurately near  $r = 0$  [9]. This leads to a discrepancy at small  $r$  between  $G_{GF}(r)$  and  $G_{EX}(r)$ . The problem can be overcome by choosing large  $M$  as we verified in  $d = 1$  and  $2$ . However, in  $d = 3$  very large  $M$  also demands prohibitively large memory. In earlier work [9,36], the correlation function  $G_{EX}(\mathbf{r})$  was sampled down to a lower resolution, and the reconstruction algorithm then proceeded with such a rescaled correlation function. This leads to a reconstructed sample  $\mathbb{S}_{GF}$  which also has a lower resolution. Such reconstructions have lower average connectivity compared to the original model [38].

Because we intend a quantitative comparison with the microstructure of  $\mathbb{S}_{\text{EX}}$  it is necessary to retain the same level of resolution. Hence we use throughout this article the original correlation function  $G_{\text{EX}}(\mathbf{r})$  without subsampling. Because  $G_{\text{EX}}(r)$  is nearly 0 for  $r > 30a$  we have truncated  $G_{\text{EX}}(r)$  at  $r = 30a$  to save computer time. The final configuration  $\mathbb{S}_{\text{GF}}$  with  $M = 256$  generated by Gaussian filtering reconstruction that is used in the comparison to experiment is displayed in Fig. 3.

### 3.4. Simulated annealing reconstruction model

The simulated annealing (SA) reconstruction model is a second method to generate a three-dimensional random microstructure with prescribed porosity and correlation function. A simplified implementation was recently discussed in Ref. [21] and we follow their algorithm here. The method generates a configuration  $\mathbb{S}_{\text{SA}}$  by minimizing the deviations between  $G_{\text{SA}}(\mathbf{r})$  and a predefined reference function  $G_0(\mathbf{r})$ . Of course in our case we have again the Fontainebleau sandstone as reference, i.e.  $G_0(\mathbf{r}) = G_{\text{EX}}(\mathbf{r})$ .

The reconstruction is performed on a cubic lattice with side length  $M = M_1 = M_2 = M_3$  and lattice spacing  $a$ . The lattice is initialized randomly with 0's and 1's such that the volume fraction of 0's equals  $\phi(\mathbb{S}_{\text{EX}})$ . This porosity is preserved throughout the simulation. For the sake of numerical efficiency the autocorrelation function is evaluated in a simplified form using [21]

$$\tilde{G}_{\text{SA}}(r)(\tilde{G}_{\text{SA}}(0) - \tilde{G}_{\text{SA}}(0)^2) + \tilde{G}_{\text{SA}}(0)^2 = \frac{1}{3M^3} \sum_{\mathbf{r}} \chi_{\mathbb{M}}(\mathbf{r})(\chi_{\mathbb{M}}(\mathbf{r} + r\mathbf{e}_1) + \chi_{\mathbb{M}}(\mathbf{r} + r\mathbf{e}_2) + \chi_{\mathbb{M}}(\mathbf{r} + r\mathbf{e}_3)), \quad (3.4)$$

where  $\mathbf{e}_i$  are the unit vectors in direction of the coordinate axes,  $r = 0, \dots, (M/2) - 1$ , and where a tilde  $\sim$  is used to indicate the directional restriction. The sum  $\sum_{\mathbf{r}}$  runs over all  $M^3$  lattice sites  $\mathbf{r}$  with periodic boundary conditions, i.e.  $r_i + r$  is evaluated modulo  $M$ .

We now perform a simulated annealing algorithm to minimize the “energy” function

$$E = \sum_r (\tilde{G}_{\text{SA}}(r) - G_{\text{EX}}(r))^2, \quad (3.5)$$

defined as the sum of the squared deviations of  $\tilde{G}_{\text{SA}}$  from the experimental correlation function  $G_{\text{EX}}$ . Each update starts with the exchange of two randomly chosen pixels, one from pore space, one from matrix space. Let  $n$  denote the number of the proposed update step. Introducing an acceptance parameter  $T_n$ , which may be interpreted as an  $n$ -dependent temperature, the proposed configuration is accepted with probability

$$p = \min\left(1, \exp\left(-\frac{E_n - E_{n-1}}{T_n E_{n-1}}\right)\right). \quad (3.6)$$

Here the energy and the correlation function of the configuration is denoted as  $E_n$  and  $\tilde{G}_{\text{SA},n}$ , respectively. The evaluation of  $\tilde{G}_{\text{SA},n}$  does not require a complete recalculation. It suffices to update the correlation function  $\tilde{G}_{\text{SA},n-1}$  of the previous configuration by

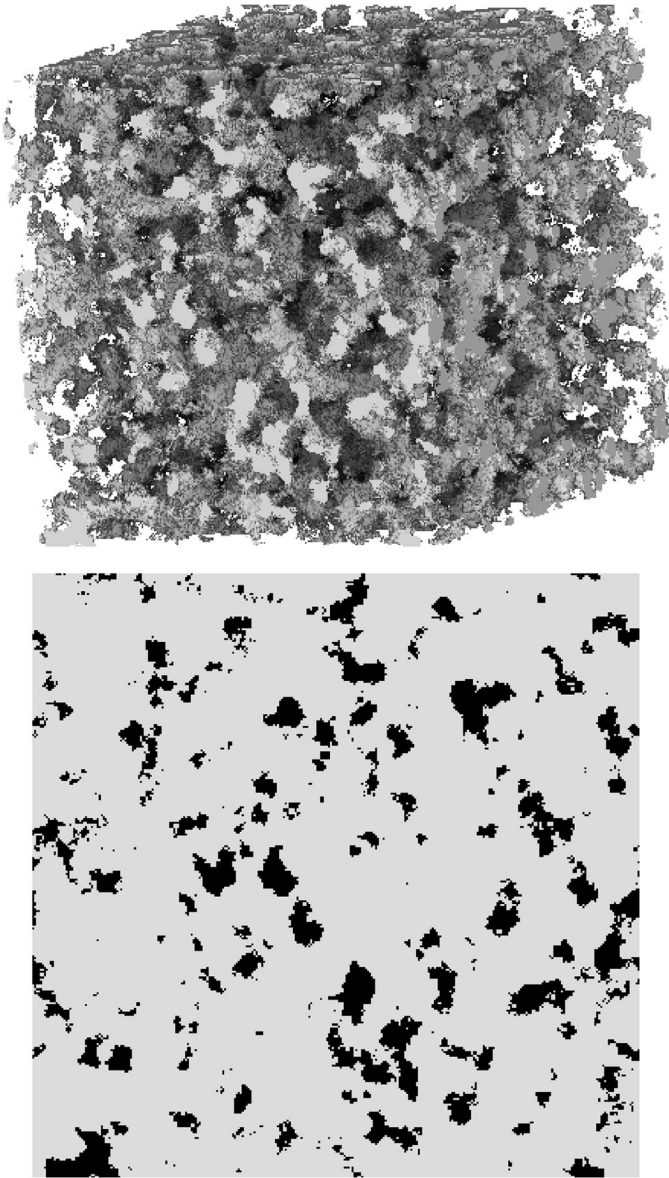


Fig. 3. Three-dimensional pore space having the same correlation function as the experimental sample of Fontainebleau sandstone (sample GF). The pore space was constructed using Gaussian random fields which are subsequently filtered. The resolution is  $a = 7.5 \mu\text{m}$ , the sample dimensions are  $M_1 = 256$ ,  $M_2 = 256$ ,  $M_3 = 256$ . The porosity is  $\phi(\mathbb{S}_{\text{GF}}) = 0.1421$ . The pore space is indicated opaque, the matrix space is transparent. The lower image shows the front plane of the sample as a two-dimensional thin section (pore space black, matrix grey).

adding or subtracting those products in (3.4) which changed due to the exchange of pixels. In case the proposed move is rejected, the old configuration is restored.

The generation of a configuration with correlation  $G_{EX}$  is achieved by lowering  $T$ . At low  $T$  the system approaches a configuration that minimizes the energy function. In our simulations we lower  $T_n$  with  $n$  as

$$T_n = \exp\left(-\frac{n}{100\,000}\right). \quad (3.7)$$

We stop the simulation when 20 000 consecutive updates are rejected. In our simulation this happened after  $2.5 \times 10^8$  updates ( $\approx 15$  steps per site). The resulting configuration  $\mathbb{S}_{SA}$  for the simulated annealing reconstruction is displayed in Fig. 4.

Our definition of the correlation function in (3.4) deserves some comment. A complete evaluation of the correlation function as defined in (2.7) requires such a great numerical expense that the algorithm is too slow to allow three-dimensional reconstructions within a reasonable time. Therefore, to increase the speed of the algorithm, the correlation function is only evaluated along the directions of the coordinate axes as indicated in (3.4). As a result of this simplification the reconstructed sample may cease to be isotropic. It will in general deviate from the reference correlation function in all directions other than those of the axes. In the special case of the correlation function of the Fontainebleau sandstone, however, this effect seems to be small (see below). This may serve as an a posteriori justification for using (3.4).

## 4. Results and discussion

We begin our presentation of the results with an analysis of traditional quantities such as porosities and correlation functions of the four samples. Then we proceed to a visual characterization of the three-dimensional images. Next we shall discuss local porosities and percolation probabilities, and finally we conclude with implications for transport properties.

### 4.1. Conventional analysis

Table 2 gives a synopsis of different properties of the four samples. The preparation of the various samples was described in detail in Section 3. The dimensions and porosities also need no further comment. Samples **GF** and **SA** were constructed to have the same correlation function as sample **EX**. This is indicated in the line labelled  $G(\mathbf{r})$ . In Fig. 5 we plot the directionally averaged correlation functions  $G(r) = (G(r, 0, 0) + G(0, r, 0) + G(0, 0, r))/3$  of the four samples where  $G(r_1, r_2, r_3) = G(\mathbf{r})$ .  $G_{DM}(r)$  differs clearly from the rest. Accidentally, however,  $G_{DM}(0, 0, r) \approx G_{EX}(0, 0, r)$ .  $G_{GF}(r)$  differs from  $G_{EX}(r)$  for small  $r$  as discussed in Section 3.3 above. Remember also that by construction  $G_{GF}(r)$  is not expected to equal  $G_{EX}(\mathbf{r})$  for  $r$  larger than 30. The discrepancy at small  $r$  reflects the quality of the linear filter, and it is also responsible for the differences of the porosity and specific internal surface. Although the

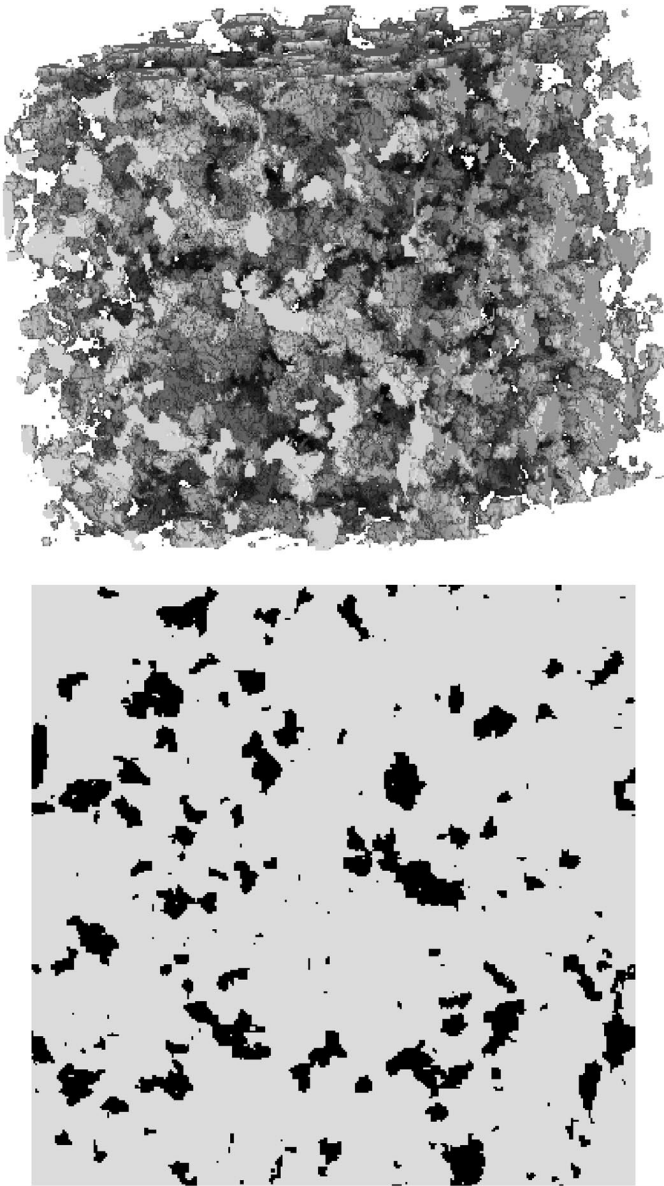


Fig. 4. Three-dimensional pore space having the same correlation function as the experimental sample of Fontainebleau sandstone (sample SA). The pore space was constructed using a simulated annealing algorithm. The resolution is  $a = 7.5 \mu\text{m}$ , the sample dimensions are  $M_1 = 256$ ,  $M_2 = 256$ ,  $M_3 = 256$ . The bulk porosity is  $\phi(\mathbb{S}_{\text{SA}}) = 0.1354$ . The pore space is indicated opaque, the matrix space is transparent. The lower image shows the front plane of the sample as a two-dimensional thin section (pore space black, matrix grey).

Table 2  
Overview of various properties for the four samples

Properties	$\mathbb{S}_{EX}$	$\mathbb{S}_{DM}$	$\mathbb{S}_{GF}$	$\mathbb{S}_{SA}$
Origin	Experiment	Diagenesis model	Gaussian field	Simulated annealing
$M_1 \times M_2 \times M_3$	$300 \times 300 \times 299$	$255 \times 255 \times 255$	$256 \times 256 \times 256$	$256 \times 256 \times 256$
$\phi(\mathbb{S})$	0.1355	0.1356	0.1421	0.1354
$G(\mathbf{r})$	$G_{EX}$	$G_{DM}$	$G_{GF} \approx G_{EX}$	$G_{SA} = G_{EX}$
$S$ from $\left. \frac{dG}{dr} \right _{r=0}$	0.078	0.082	0.125	0.083
Isotropy	$xyz$	$xy$	$xyz$	$xyz$
Isolated $\mathbb{M}$	No	No	Yes	Yes
Pore surface	Smooth	Smooth	Rough	Rough
$L^*$	35	25	23	27
Connectivity	$xyz$	$xyz$	$xyz$	$xyz$
$1 - \lambda_c(0.1355, L^*)$	0.0045	0.0239	0.3368	0.3527

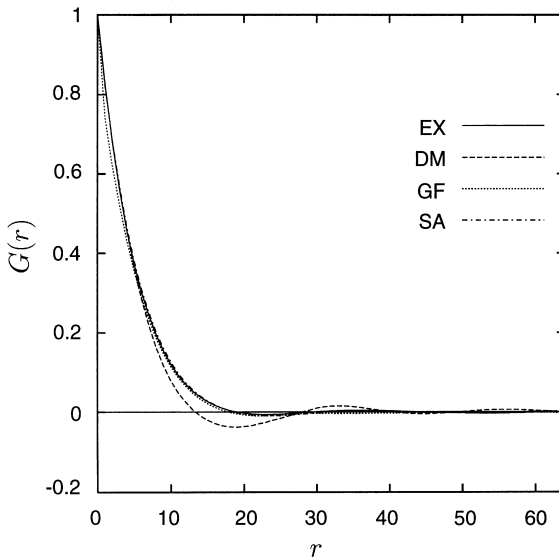


Fig. 5. Averaged directional correlation functions  $G(r) = (G(r, 0, 0) + G(0, r, 0) + G(0, 0, r))/3$  of all four samples.

reconstruction method of sample  $\mathbb{S}_{SA}$  is intrinsically anisotropic the correlation function of sample **SA** agrees also in the diagonal directions with that of sample **EX**. Sample  $\mathbb{S}_{DM}$  on the other hand has an anisotropic correlation function.

If two samples have the same correlation function they are also expected to have the same specific internal surface as calculated from

$$S = -4\langle\phi\rangle(1 - \langle\phi\rangle)\left. \frac{dG(r)}{dr} \right|_{r=0}. \tag{4.1}$$

The line in Table 2 labelled  $S$  gives the specific internal surfaces.

If one defines a decay length by the first zero of the correlation function then the decay length is roughly  $18a$  for samples EX, GF and SA. For sample DM it is somewhat smaller mainly in the  $x$ - and  $y$ -direction. The correlation length, which will be of the order of the decay length, is thus relatively large compared to the system size. Together with the fact that the percolation threshold for continuum systems is typically around 0.15 this might explain why models GF and SA are connected in spite of their low value of the porosity.

In summary, the samples  $S_{GF}$  and  $S_{SA}$  were constructed to be indistinguishable with respect to porosity and correlations from  $S_{EX}$ . The imperfection of the reconstruction method for sample GF, however, accounts for the deviations of its correlation function at small  $r$  from that of sample EX.

#### 4.2. Visual inspection of images

We now collect results from a visual comparison. Visual inspection of Figs. 1–4 reveals that none of the models  $S_{DM}$ ,  $S_{GF}$  or  $S_{SA}$  resemble closely the experimental microstructure  $S_{EX}$ . This applies in particular to samples GF and SA which were constructed to match the traditional geometrical characteristics of sample EX, such as porosity, specific surface and correlation function.

Figs. 1–4 suggest that samples  $S_{GF}$  and  $S_{SA}$  have isolated islands of matrix space although this cannot be seen directly because the pore space is rendered opaque. Isolated islands of matrix space cannot exist in a real porous medium such as sample EX. They are also absent in the compaction and diagenesis model DM. The comparison is indicated in the line labelled “isolated M” in Table 2. The pore surfaces in samples GF and SA are much rougher than in samples EX and DM. Sample DM appears visually more homogeneous than the other samples. Although there is no anisotropy visible for sample DM from Fig. 2 its connectivity properties will be found below to be strongly anisotropic.

In summary the traditional characteristics such as porosity, specific surface and correlation functions are insufficient to distinguish different microstructures. Visual inspection of the pore space by the human eye indicates that samples GF and SA have a similar structure which, however, differs from the structure of sample EX. Although sample DM resembles sample EX more closely with respect to surface roughness it differs visibly in the shape of the grains.

#### 4.3. Local porosity analysis

We turn to an analysis of the fluctuations in local porosities. The differences in visual appearance of the microstructures find a quantitative expression here.

The local porosity distributions  $\mu(\phi, 20)$  of the four samples at  $L=20a$  are displayed as the solid lines in Figs. 6–9. The ordinates for these curves are plotted on the right vertical axis. The figures show that the original sample exhibits stronger porosity fluctuations than the three model samples except for sample SA which comes close.

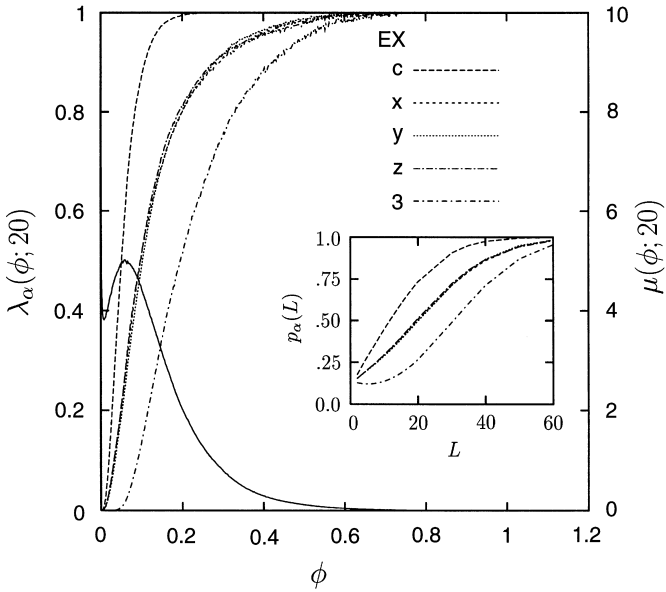


Fig. 6. Local percolation probabilities  $\lambda_\alpha(\phi, 20)$  (broken curves, values on left axis) and local porosity distribution  $\mu(\phi, 20)$  (solid curve, values on right axis) at  $L = 20$  for sample EX. The inset shows the function  $p_\alpha(L)$ . The line styles corresponding to  $\alpha = c, x, y, z, 3$  are indicated in the legend.

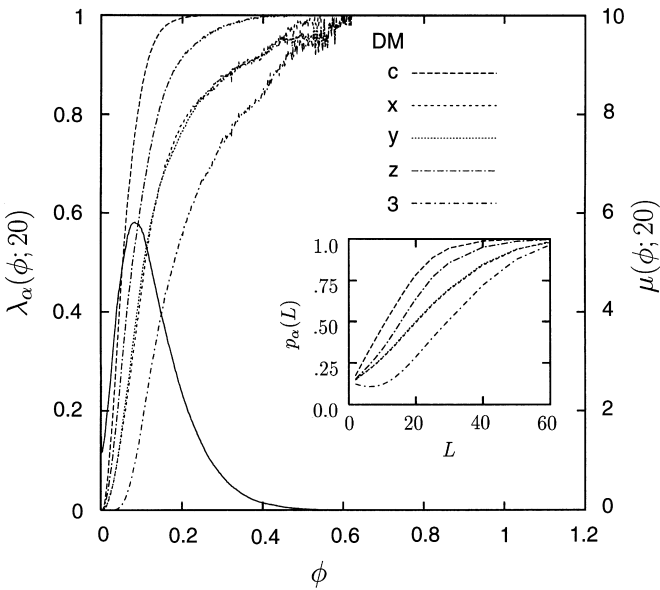


Fig. 7. Local percolation probabilities  $\lambda_\alpha(\phi, 20)$  (broken curves, values on left axis) and local porosity distribution  $\mu(\phi, 20)$  (solid curve, values on right axis) at  $L = 20$  for sample DM. The inset shows the function  $p_\alpha(L)$ . The line styles corresponding to  $\alpha = c, x, y, z, 3$  are indicated in the legend.

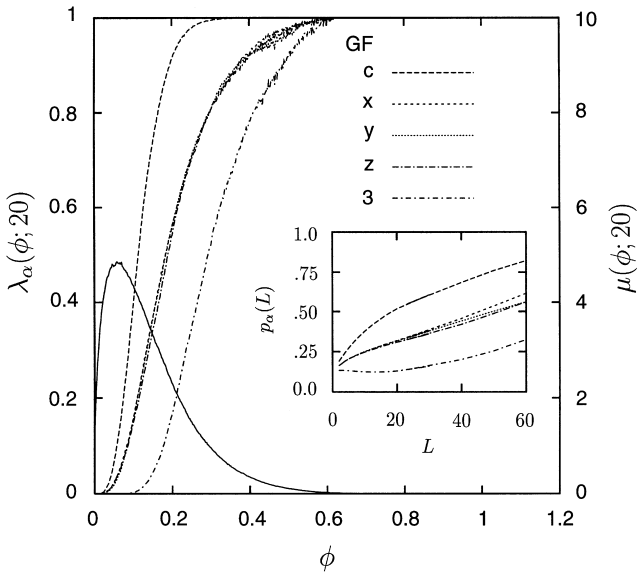


Fig. 8. Local percolation probabilities  $\lambda_z(\phi, 20)$  (broken curves, values on left axis) and local porosity distribution  $\mu(\phi, 20)$  (solid curve, values on right axis) at  $L = 20$  for sample GF. The inset shows the function  $p_z(L)$ . The line styles corresponding to  $\alpha = c, x, y, z, 3$  are indicated in the legend.

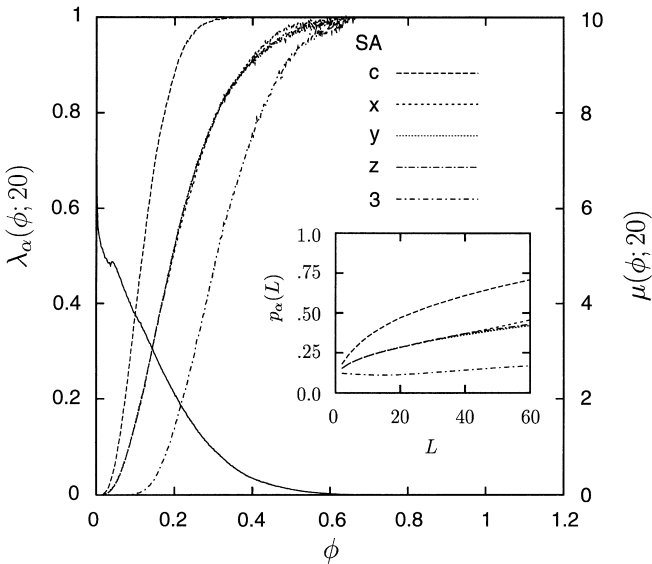


Fig. 9. Local percolation probabilities  $\lambda_z(\phi, 20)$  (broken curves, values on left axis) and local porosity distribution  $\mu(\phi, 20)$  (solid curve, values on right axis) at  $L = 20$  for sample SA. The inset shows the function  $p_z(L)$ . The line styles corresponding to  $\alpha = c, x, y, z, 3$  are indicated in the legend.

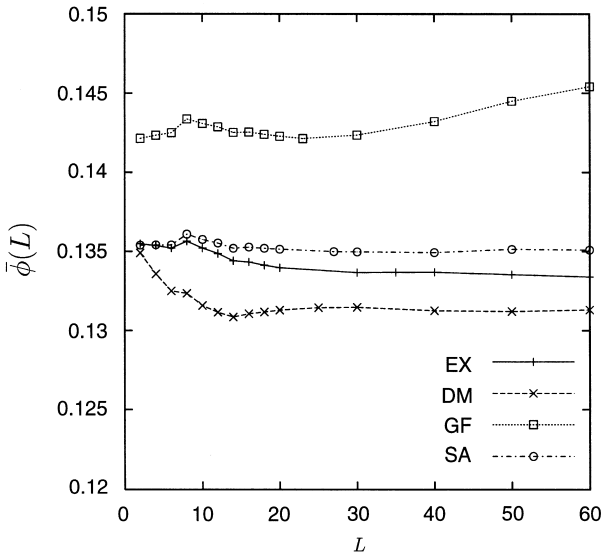


Fig. 10. Average local porosities for sample EX (solid line with tick) DM (dashed line with cross) GF (dotted line with square), and SA (dash-dotted line with circle).

Sample DM has the narrowest distribution which indicates that it is most homogeneous. Figs. 6–9 show also that the component at the origin,  $\mu(0,20)$ , is largest for sample EX, and smallest for sample GF. For samples DM and SA the values of  $\mu(0,20)$  are intermediate and comparable. Plotting  $\mu(0,L)$  as a function of  $L$  we find that this remains true for all  $L$ . These results indicate that the experimental sample EX is more strongly heterogeneous than the models, and that large regions of matrix space occur more frequently in sample EX. A similar conclusion may be drawn from the variance of local porosity fluctuations which will be studied below. The conclusion is also consistent with the results for  $L^*$  shown in Table 2.  $L^*$  gives the sidelength of the largest cube that can be fit into matrix space, and thus  $L^*$  may be viewed as a measure for the size of the largest grain. Table 2 shows that the experimental sample has a larger  $L^*$  than all the models. It is interesting to note that plotting  $\mu(1,L)$  versus  $L$  also shows that the curve for the experimental sample lies above those for the other samples for all  $L$ . Thus, also the size of the largest pore and the pore space heterogeneity are largest for sample EX. If  $\mu(\phi, L^*)$  is plotted for all four samples one finds two groups. The first group is formed by samples EX and DM, the second by samples GF and SA. Within each group the curves  $\mu(\phi, L^*)$  nearly overlap, but they differ strongly between them.

Figs. 10–12, exhibit the dependence of the local porosity fluctuations on  $L$ . In Fig. 11 we plot the variance of the local porosity fluctuations, defined in Eq. (2.12) as function of  $L$ . The variances for all samples indicate an approach to a  $\delta$ -distribution according to Eq. (2.14). Again sample DM is most homogeneous in the sense that

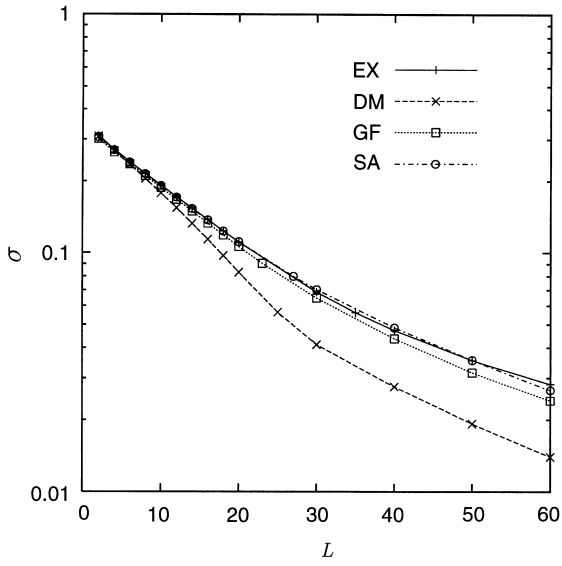


Fig. 11. Variance of local porosities for sample EX (solid line with tick) DM (dashed line with cross) GF (dotted line with square), and SA (dash-dotted line with circle).

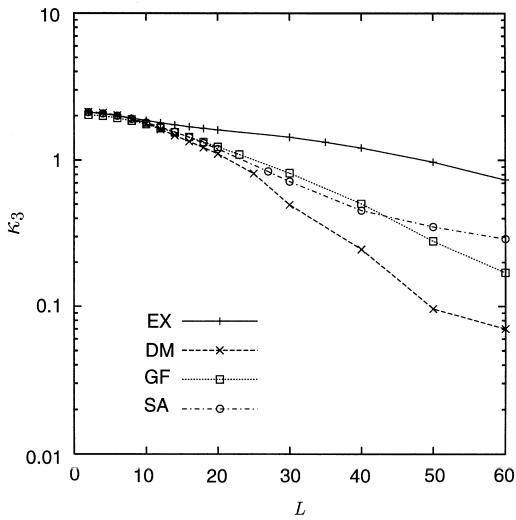


Fig. 12. Skewness of local porosities for sample EX (solid line with tick) DM (dashed line with cross) GF (dotted line with square), and SA (dash-dotted line with circle).

its variance is smallest. The agreement between samples EX, GF and SA reflects the agreement of their correlation functions, and is expected by virtue of Eq. (2.12). Fig. 12 shows the skewness as a function of  $L$  calculated from

$$\kappa_3(L) = \frac{\overline{(\phi(L) - \bar{\phi}(L))^3}}{\sigma(L)^3}, \quad (4.2)$$

where  $\sigma(L)$  is the variance defined in Eq. (2.12).  $\kappa_3$  characterizes the asymmetry of the distribution, and the difference between the most probable local porosity and its average. Again samples GF and SA behave similarly, but sample DM and sample EX differ from each other, and from the rest.

At  $L = 4a$  the local porosity distributions  $\mu(\phi, 4)$  show small spikes at equidistantly spaced porosities for samples EX and DM, but not for samples GF and SA. The spikes indicate that models EX and DM have a smoother surface than models GF and SA. For smooth surfaces and small measurement cells porosities corresponding to an interface intersecting the measurement cell occur with higher frequency, and this gives rise to spikes. The presence of isolated islands of pore or matrix space reduces these spikes. It is unclear at present whether the spikes persist when the measurement cells are chosen to be nonoverlapping.

#### 4.4. Local percolation analysis

Visual inspection of Figs. 1–4 did not allow us to recognize the degree of connectivity of the various samples. A quantitative characterization of the connectivity is provided by the local percolation probabilities [30,35], and it is here that the samples differ most dramatically.

All the four samples are globally connected in all three directions. This, however, does not imply that the samples have similar or comparable connectivity. The last line in Table 2 gives the fraction of blocking cells at the porosity 0.1355 and for  $L^*$ . It gives a first indication that the connectivity of samples SA and GF is, in fact, much poorer than that of the experimental sample EX.

Figs. 6–9 give a more complete account of the situation by exhibiting  $\lambda_\alpha(\phi, 20)$  for  $\alpha = 3, c, x, y, z$  for all four samples. First, one notes that sample DM is strongly anisotropic in its connectivity. It has a higher connectivity in the  $z$ -direction than in the  $x$ - or  $y$ -direction. This might be due to the anisotropic compaction process.  $\lambda_z(\phi, 20)$  for sample DM differs from that of sample EX although their correlation functions in the  $z$ -direction are very similar. The  $\lambda$ -functions for samples EX and DM rise much more rapidly than those for samples GF and SA. The inflection point of the  $\lambda$ -curves for samples EX and DM is much closer to the most probable porosity (peak) than in samples GF and SA. All of this indicates that connectivity in cells with low porosity is higher for samples EX and DM than for samples GF and SA. In samples GF and SA only cells with high porosity are percolating on average. In sample DM the curves  $\lambda_x, \lambda_y$  and  $\lambda_3$  show strong fluctuations for  $\lambda \approx 1$  at values of  $\phi$  much larger than the  $\langle \phi \rangle$  or  $\phi(\mathbb{S}_{DM})$ . This indicates a large number of high porosity cells

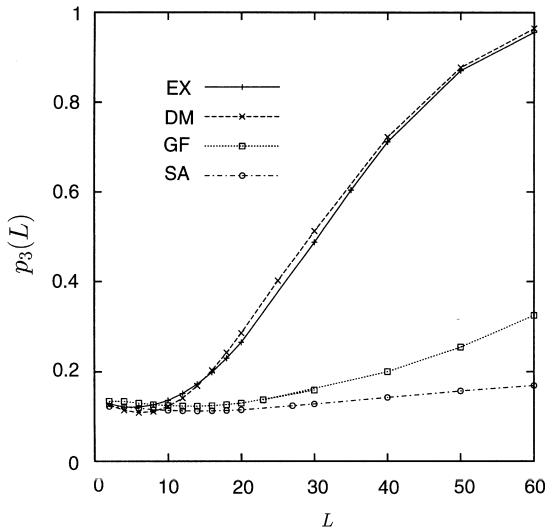


Fig. 13.  $p_3(L)$  for sample EX (solid line with tick) DM (dashed line with cross) GF (dotted line with square), and SA (dash-dotted line with circle).

which are nevertheless blocked. The reason for this is perhaps that the linear compaction process in the underlying model blocks horizontal pore throats and decreases horizontal spatial continuity more effectively than in the vertical direction, as shown in [28], Table 1 p. 142.

The absence of spikes in  $\mu(\phi, 4)$  for samples GF and SA combined with the fact that cells with average porosity ( $\approx 0.135$ ) are rarely percolating suggests that these samples have a random morphology similar to percolation.

#### 4.5. Implications for transport properties

The connectivity analysis of local porosity theory allows to make some predictions for transport properties (such as conductivity or permeability) without actually calculating them. A detailed comparison between the predictions of local porosity theory and exact calculation of transport properties will appear elsewhere [39]. These predictions are made by calculating the total fraction of percolating cells from Eq. (2.18). The insets in Figs. 6–9 show the functions  $p_\alpha(L) = \overline{\lambda_\alpha(\phi, L)}$  for  $\alpha = 3, x, y, z, c$  for each sample. The curves for samples EX and DM are similar but differ from those for samples GF and SA. In Fig. 13 we plot the curves  $p_3(L)$  of all four samples in a single figure. The samples fall into two groups  $\{\text{EX, DM}\}$  and  $\{\text{GF, SA}\}$  that behave very differently. Fig. 13 shows that reconstruction methods [9,21] based on correlation functions do not reproduce the connectivity properties of porous media. As a consequence, within the effective medium approximation of local porosity theory [30] samples GF and SA would both yield much lower permeabilities or conductivities than those of

samples EX and DM. Based on these results it appears questionable whether correlation function reconstruction can produce reliable models for the prediction of transport.

## Acknowledgements

The authors are grateful to Dr. David Stern, (Exxon Research Production Company) for providing the experimental data set, and to the Deutsche Forschungsgemeinschaft for financial support.

## References

- [1] I. Fatt, The network model of porous media I. capillary pressure characteristics, *AIME Petroleum Trans.* 207 (1956) 144.
- [2] A. Scheidegger, *The Physics of Flow Through Porous Media*, University of Toronto Press, Toronto, 1974.
- [3] I. Chatzis, F. Dullien, Modelling pore structure by 2-d and 3-d networks with applications to sandstones, *J. Canad. Petroleum Technol.* Jan-Mar 1977, p. 97.
- [4] J. Ziman, *Models of Disorder*, Cambridge University Press, Cambridge, 1982.
- [5] J. Roberts, L. Schwartz, Grain consolidation and electrical conductivity in porous media, *Phys. Rev. B* 31 (1985) 5990.
- [6] C. Jacquin, P. Adler, Fractal porous media II: geometry of porous geological structures, *Transport Porous Media* 2 (1987) 28.
- [7] L. Schwartz, S. Kimminau, Analysis of electrical conduction in the grain consolidation model, *Geophysics* 52 (1987) 1402.
- [8] U. Oxaal, Fractal viscous fingering in inhomogeneous porous models, *Phys. Rev. A* 44 (1991) 5038.
- [9] P. Adler, *Porous Media*, Butterworth-Heinemann, Boston, 1992.
- [10] R. Blumenfeld, S. Torquato, Coarse graining procedure to generate and analyze heterogeneous materials: theory, *Phys. Rev. E* 48 (1993) 4492.
- [11] M. Sahimi, *Flow and Transport in Porous Media and Fractured Rock*, VCH, Weinheim, Verlagsgesellschaft mbH, 1995.
- [12] J. Feder, T. Jøssang, Fractal patterns in porous media flow, in: C. Barton, L. Pointe (Eds.), *Fractals in Petroleum Geology and Earth Processes*, Plenum Press, New York, 1995, p. 179.
- [13] D. Jeulin, A.L. Coënt, Morphological modeling of random composites, in: K. Markov (Ed.), *Continuum Models and Discrete Systems*, World Scientific Publishing Company, Singapore, 1996, p. 199.
- [14] J. Andrade, M. Almeida, J.M. Filho, S. Havlin, B. Suki, H. Stanley, Fluid flow through porous media: the role of stagnant zones, *Phys. Rev. Lett.* 79 (1997) 3901.
- [15] P. Øren, S. Bakke, O. Arntzen, Extending predictive capabilities to network models, *SPE J.*, vol. 3 1998, p. 324.
- [16] R. Hilfer, Transport and relaxation phenomena in porous media, *Adv. Chem. Phys.* XCII (1996) 299.
- [17] C. Andraud, A. Beghdadi, E. Haslund, R. Hilfer, J. Lafait, B. Virgin, Local entropy characterization of correlated random microstructures, *Physica A* 235 (1997) 307.
- [18] F. Boger, J. Feder, R. Hilfer, T. Jøssang, Microstructural sensitivity of local porosity distributions, *Physica A* 187 (1992) 55.
- [19] C. van Siclén, Information entropy of complex structures, *Phys. Rev. E* 56 (1997) 5211.
- [20] J. Quiblier, A new three dimensional modeling technique for studying porous media, *J. Colloid Interface Sci.* 98 (1984) 84.
- [21] C. Yeong, S. Torquato, Reconstructing random media, *Phys. Rev. E* 57 (1998) 495.
- [22] C. Yeong, S. Torquato, Reconstructing random media II. three-dimensional media from two-dimensional cuts, *Phys. Rev. E* 58 (1998) 224.
- [23] T. Bourbie, B. Zinszner, Hydraulic and acoustic properties as a function of porosity in Fontainebleau sandstone, *J. Geophys. Res.* 90 (1995) 11 524.

- [24] T. Bourbie, O. Coussy, B. Zinszner, *Acoustics of Porous Media*, Editions Technip, Paris, 1987.
- [25] J. Thovert, J. Salles, P. Adler, Computerized characterization of the geometry of real porous media: their discretization, analysis and interpretation, *J. Microscopy* 170 (1993) 65.
- [26] G. Stell, Mayer-montroll equations (and some variants) through history for fun and profit, in: M. Shlesinger, G. Weiss (Eds.), *The Wonderful World of Stochastics*, Amsterdam, Elsevier, 1985, p. 127.
- [27] F. Dullien, *Porous Media – Fluid Transport and Pore Structure*, Academic Press, San Diego, 1992.
- [28] S. Bakke, P. Øren, 3-d pore-scale modeling of sandstones and flow simulations in pore networks, *SPE J.* 2 (1997) 136.
- [29] R. Hilfer, Local porosity theory for flow in porous media, *Phys. Rev. B* 45 (1992) 7115.
- [30] R. Hilfer, Geometric and dielectric characterization of porous media, *Phys. Rev. B* 44 (1991) 60.
- [31] R. Hilfer, Geometry, dielectric response and scaling in porous media, *Physica Scripta* T44 (1992) 51.
- [32] R. Hilfer, Local porosity theory for electrical and hydrodynamical transport through porous media, *Physica A* 194 (1993) 406.
- [33] B. Hansen, E. Haslund, R. Hilfer, B. Nøst, Dielectric dispersion measurements of salt water saturated porous glass compared with local porosity theory, *Mater. Res. Soc. Proc.* 290 (1993) 185.
- [34] R. Hilfer, B. Nøst, E. Haslund, Th. Kautzsch, B. Virgin, B.D. Hansen, Local porosity theory for the frequency dependent dielectric function of porous rocks and polymer blends, *Physica A* 207 (1994) 19.
- [35] B. Biswal, C. Manwart, R. Hilfer, Three-dimensional local porosity analysis of porous media, *Physica A* 255 (1998) 221.
- [36] P. Adler, C. Jacquin, J. Quiblier, Flow in simulated porous media, *Int. J. Multiphase Flow* 16 (1990) 691.
- [37] J. Yao, P. Frykman, F. Kalaydjian, P. Thovert, P. Adler, High-order moments of the phase function for real and reconstructed model porous media: a comparison, *J. Colloid Interface Sci.* 156 (1993) 478.
- [38] B. Biswal, R. Hilfer, Microstructure analysis of reconstructed porous media, *Physica A* 266 (1999) 307.
- [39] J. Widjajakusuma, B. Biswal, R. Hilfer, Quantitative prediction of effective material properties of heterogeneous media, *Comput. Mater. Sci.* 1999, in press.